BMES BIOMEDICAL ENGINEERING SOCIETY

ORIGINAL ARTICLE

Computer Aided Intracranial Aneurysm Treatment Based on 2D/3D Mapping, Virtual Deployment and Online Distal Marker Detection

Nicolas Dazeo[1] · José Ignacio Orlando[1] · Camila García[1] · Romina Muñoz[1] · Laura Obrado[2] · Hector Fernandez[2] · Jordi Blasco[3] · Luis San Román[3] · Juan M. Macho[3] · Andreas Ding[4] · Raphael Utz[4] · Ignacio Larrabide[1,2]

Abstract

Purpose To introduce a computational tool for peri-interventional intracranial aneurysm treatment guidance that maps preoperative planning information from simulation onto real-time X-Ray imaging.

Methods Preoperatively, multiple flow diverter (FD) devices are simulated based on the 3D mesh of the vessel to treat, to choose the optimal size and location. In the peri-operative stage, this 3D information is aligned and mapped to the continuous 2D-X-Ray scan feed from the operating room. The current flow diverter position in the 3D model is estimated by automatically detecting the distal FD marker locations and mapping them to the treated vessel. This allows to visually assess the possible outcome of releasing the device at the current position, and compare it with the one chosen pre-operatively.

Results The full pipeline was validated using retrospectively collected biplane images from four different patients (5 3D-DSA datasets in total). The distal FD marker detector obtained an average F1-score of 0.67 ($\pm$0.224) in 412 2D-X-Ray scans. After aligning 3D-DSA + 2D-X-Ray datasets, the average difference between simulated and deployed positions was 0.832 mm ($\pm$0.521 mm). Finally, we qualitatively show that the proposed approach is able to display the current location of the FD compared to their pre-operatively planned position.

Conclusions The proposed method allows to support the FD deployment procedure by merging and presenting preoperative simulation information to the interventionists, aiding them to make more accurate and less risky decisions.

Keywords Cerebral aneurysm · Treatment guidance · Alignment · 3D-DSA · 2D-X-ray · Real time

Introduction

Between 3% to 5% of the population are estimated to have at least one intracranial aneurysm [1], with factors such as sex and age being factors of higher incidence [2–4]. These lesions have an associated rupture risk of 30% to 40%,

✉ Nicolas Dazeo
   ndazeo@pladema.exa.unicen.edu.ar

   Ignacio Larrabide
   larrabide@exa.unicen.edu.ar

1 Yatiris Research Group, PLADEMA Institute, CONICET-UNICEN, Campus Universitario, Tandil, Argentina

2 Mentice S. L., Barcelona, Spain

3 Department of Neuroradiology, Hospital Clinic, Barcelona, Spain

4 Acandis, GmbH, Pforzheim, Germany

which leads to subarachnoid hemorrhage with significant morbidity and mortality rates [5–7]. To mitigate this peril, patients with intracranial aneurysms are recommended to undergo endovascular treatments with coils, stents, and/or flow diverters (FDs) [8]. While endovascular devices often result in incomplete occlusion or recanalization, FDs induce both intra-aneurysmal blood stagnation and reconstruction of the parent artery [9]. Treatment success heavily relies on accurately selecting the optimal device and deployment location. The FD final length, and therefore the proximal end position, is not well known when the deployment starts. This uncertainty could lead improper FD sizing, misplacement, or misalignment and result in complications such as covered side branches, inadequate aneurysm occlusion, poor wall apposition, or FD migration [10–15].

To overcome these challenges, preoperative planning is performed by computationally simulating the intervention on the patient's vascular geometry extracted from a preoperative 3D-DSA scan [16–19]. These analyses enable experts

🖄 Springer

to virtually "try" different FDs in a safe, controlled environment, allowing them to explore alternative positions and sizes without risking the patient. Hence, the final outcomes can be evaluated *in silico* based on various criteria, including hemodynamic simulations, adverse events requiring re-treatment, occlusion rate, and occlusion time [20–24], and chose optimal configurations in advance based on these results.

While simulations assist in preoperative planning, treatment outcomes always depend on events occurring during the procedure itself [25]. To guide themselves during the intervention, specialists use a continuous live stream of 2D-X-Ray images in which radiopaque markers located at distal positions of the FD (visualized as dark points, Fig. 1) are used as cues of the location of the FD. However, the geometry of the treated vessel is not observable unless a contrast agent is injected. When that occurs, interventionists can visualize a 2D roadmap of the vasculature by digitally subtracting images before and after contrast, which remains as a fixed view-point 2D image. Nevertheless, this reference needs to be regenerated each time the C-arm is re-positioned. Thus, when 2D X-ray images are acquired during the procedure, interventionists used this technique of contrast injection to obtain the roadmap only when it is strictly necessary, heavily relying on their own knowledge

of the patient's anatomy during most of the intervention to determine the optimal device deployment location. There is therefore a lack of tools that seamlessly integrates preoperative and peri-operative information to support this critical decision-making process.

In this paper we introduce a methodology to address this particular challenge. First, images acquired during the intervention are co-registered with the pre-operative vascular structure. While numerous studies have proposed using the C-arm location to register 2D-X-Ray scans to pre-intervention 3D images [26–28], these mapping techniques have been primarily focused on visualization, and not exploited for real-time monitoring of device positioning. Alternatively, we propose to accurately identify the FD's position in real-time using deep learning, and then leverage this approach to map it to its precise location onto the 3D vessel geometry. Current detection approaches combine classical image processing techniques to identify candidate points first, and statistical learning methods to eliminate false positive detections [29, 30]. Alternatively, other more recent methods have shown improved results using U-Net-based deep learning architectures [31]. All these existing alternatives have been applied though to images from anatomical regions different than the brain [32, 33].
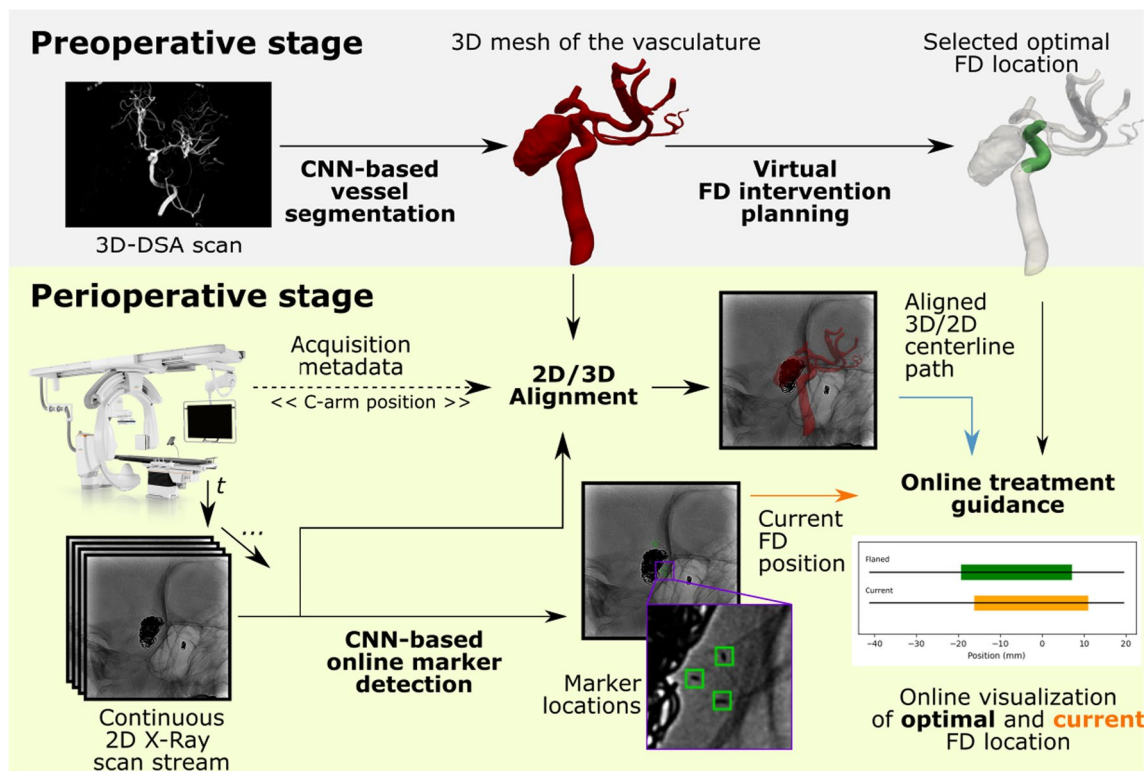
Fig. 1 Schematic representation of the proposed pipeline. Pre-operatively, the patient's vasculature is segmented from a 3D-DSA scan. A virtual intervention planning is performed using one or more FD sizes are simulated on the vessel to choose the optimal device size and location. During the intervention, a continuous stream of 2D-X-Ray images is captured using a C-arm, and the vascular geometry is automatically aligned with them. Furthermore, a CNN model is used to identify the positions of the distal FD markers, which are mapped onto the vessel to allow determining the current FD position and compare it to the originally planned deployment location

Our method is designed to enable real-time guidance during the intervention, combining through a straightforward 2D/3D alignment strategy the results of a U-Net-based FD marker detector with the 3D geometry of the patient's vascular anatomy and the results of the offline virtual planning stage. To the best of our knowledge, this is the first approach that integrates preoperative FD simulations with peri-operative imaging for computer-assisted treatment of intracranial aneurysms, providing interventionists with valuable guidance for precisely positioning the device at the predetermined optimal deployment site.

Methods

Figure 1 presents an overview of our pipeline. A pre-trained convolutional neural network (CNN) is first applied on the preoperative 3D-DSA scan to extract the vessel geometry (Sect. 2.1). The resulting anatomy is used to simulate a FD treatment along its centerline, using a specific device with a given size (Sect. 2.2). This simulation allows the clinician to select the optimal FD size and deployment location, which are made available during the online treatment to aid the interventionist in positioning the FD more accurately.

As typically done for these interventions, bi-planar 2D-X-Ray images are continuously acquired during treatment. The 3D vessel geometry is superimposed in these scans, using the acquisition metadata –i.e. the C-arm position–for precise alignment of the vascular structure with the input image (Sect. 2.4). Simultaneously, a CNN model is applied to automatically detect the position of the FD markers in the 2D images (Sect. 2.3). These points are mapped to the 3D centerline of the vasculature and serve as landmarks to determine the current position of the distal end of the FD during its positioning and release (Sect. 2.4). To provide a more comprehensive representation to the interventionists, both the current and optimal FD locations are depicted together using a separate visualization tool.

CNN-Based Vessel Segmentation and Centerline Extraction

To retrieve the vascular geometry from the 3D-DSA scans, we used the exact same voxel-based segmentation approach presented in [19], which features a U-Net-like architecture trained with manually segmented images and a combination of standard and centerline based Dice losses.

This U-Net is a fully convolutional neural network based on nnU-Net[34]. It starts from the 3D-DSA image as input. It performs 4 down-sampling operations, where spatial dimensions are divided to a half, and convolutions start with 32 kernels duplicating them in each layer. Then, 4 up-sampling operations are followed with the same dimensions for each layer. Down-sampling is performed with strided convolutions and up-sampling with transposed convolutions. Each convolutional layer is followed by instance normalisation and a leaky ReLU non-linear function. Finally, an argmax function is applied to the output of the last layer of the network, obtaining a binary 3D image of the same size of the input where a 1 represents a pixel inside the vessel and a 0 otherwise.

The vessel centerline for simulation is retrieved using the Vascular Modeling Toolkit (VMTK) [35] on the 3D surface of the vessels. The centerlines are determined as weighted shortest paths traced between the extremal points, obtained using the marching cubes algorithm. To determine if the points are in the center of a vessel, they are considered as the centers of maximal inscribed spheres. The method also stores for each point the calculated Local Morphology Information (LMI), as the maximum inscribed radius, curvature, and abscissas.

Virtual FD Intervention Planning from 3D Vascular Geometry

The virtual treatment planning stage is performed using the FD deployment method described in [17], as available in the ANKYRAS platform (Mentice S.L., Barcelona, Spain).[1] The method takes as input the computed centerline from Sec. 2.1, the nominal length of the FD (i.e. the length when deployed outside the vessel, in free space) and a Length Change Function (LCF) predefined for each device model. The LCF computes for the LMI how much of a nominal length of the FD is required to cover the space between one point and its neighbours. The algorithm starts from each possible distal position along the centerline and estimate the total length of the FD if the deploy starts at that point by applying the LCF on the LMI of the consecutive points until the complete FD is deployed.

CNN-Based Online FD Marker Detection

We address the marker detection problem by formulating it as a generic object detection task. Several deep learning models to approach this problem require a significant amount of annotated data, such as bounding boxes encompassing each marker. This is challenging in our domain, given the cost of obtaining a sufficiently large and diverse set of X-ray images with annotated markers, especially given the small size of these landmarks.

To overcome this limitation, we followed a multi-instance approach similar to the one applied in [36] for junction detection in retinal images, in this case mapping the marker

---

1 https://www.ankyras.com/.

detection problem to a segmentation task. In this setting, circular masks with a radius of 3 pixels are assigned to each marker, and a neural network is trained to identify these instances in a pixel-wise manner. This approach allows us to leverage encoder-decoder architectures such as the U-Net [31], which have shown promising results in regimes of limited available data [32, 33].

We tested 3 different architectures for marker detection, including a baseline U-Net that segment markers into 4 classes–FD markers, cathether markers, no return marker and pusher–(U-Net segm+class4), an additional one that segment markers into 2 classes–FD marker, other marker–(U-Net segm+class2), and a two-stage U-Net that first segments markers and then classifies them according to their type (U-Net two-stage). In all cases, the backbone network consisted of six downstream and upstream convolutional blocks, each comprising two convolutional layers followed by a rectified linear unit (ReLU) activation unit and batch normalization, respectively. The upstream block in particular is a convolutional block preceded by an nearest neighbor upsampling operation. For the U-Net two-stage model, we balanced the amount of filters in each stage to approximately match the capacity of the baseline architectures. In all cases, models were trained using 1600 patches of size 256×256 pixels, randomly selected from the 2D-X-Ray images in the training set. A standard cross-entropy loss was used for training, minimized using Adam optimization with a fixed learning rate of 0.01.

Computer-Aided Treatment with Online Guidance Through 2D/3D Image Matching

2D-X-Ray images are input in DICOM format, which includes both image data and its associated metadata. We use the latter to align the biplane images from the stream with the corresponding pre-operative 3D image. To ensure an accurate 3D to 3D mapping of landmarks and to render all data from a consistent perspective, we create two 3D scenes that match the configuration of the C-arm at the time of image acquisition. These are produced using Algorithm 1.

Algorithm 1 Matching 3D scenes to C-arm configuration

Input:
    Source position (x_s, y_s, z_s)
    Patient position (x_p, y_p, z_p)
    Row spacing `rspacing`
    Vertical resolution `vedge`
    Source-to-detector distance `sourceTodetector`
Output:
    Camera parameters: Focal point, `ViewUp` vector, `Position` vector, `ViewAngle`

1. Set Focal point to the origin: $(x = 0, y = 0, z = 0)$
2. Set `ViewUp` vector parallel to the z-axis
3. Initialize the `Position` vector as follows:

   - $y_p =$ distance from source to patient
   - $x_p = 0$
   - $z_p = 0$

4. Rotate the `Position` vector:
   (a) Rotate it by the primary angle in the z-axis
   (b) Rotate it by the secondary angle in the y-axis
5. Calculate `ViewAngle` $= \arctan\left(2 \cdot \frac{\texttt{rspacing} \times \texttt{vedge}}{\texttt{sourceTodetector}}\right)$

Table 1 Marker detection results obtained by each model alternative on each test sets

CNN model	Segmentation test set			Pipeline test set		
	F1	Pr	Re	F1	Pr	Re
U-Net segm+class4	0.67	0.68	0.66	0.47	0.85	0.33
U-Net segm+class2	0.30	0.22	0.46	0.29	0.47	0.21
U-Net two-stage	0.53	0.46	0.62	0.15	0.13	0.19

At the same time, markers detected in the 2D-X-Ray images are mapped to the 3D rendering scene and subsequently to the 3D vessel geometry. To achieve this, two lines are traced in the 3D space for each detected marker, in a way that they pass through each marker and extend perpendicularly to the corresponding 2D biplane image. The exact point in which they intersect with the underlying 3D rendering scene represents the approximate 3D position of the marker within the scene. Additionally, we determine the closest point on the 3D centerline to the mapped markers, representing the current location of the associated distal or proximal end of the FD. This precise localization of the flow diverter's position during the treatment procedure enables accurate placement and continuous monitoring of the device.

Materials

To evaluate and validate the effectiveness of the proposed pipeline, we used a combination of 5 pairs of pre-operative 3D-DSA scans and their corresponding biplane 2D-X-Ray images. Three of them captured with a Philips Medical Systems AlluraXper and two with a Siemens AXIOM-Artis. All scans were acquired at the end of the intervention, where the FD and associated markers are clearly visible, and were treated with an Acandis Derivo® Braided, self-expanding FD, which is equipped with three radiopaque markers on both distal and proximal ends.

The marker detection models were trained and evaluated using 573 X-Ray images retrospectively collected and anonymized by Acandis®. Scans were acquired using different machines and resolutions ranging from 256 to 1024 pixels. The set was randomly divided into training (70%), validation (20%), and test (10%, namely Segmentation Test Set). Additionally, we used the 2D X-Ray scans applied to evaluate the matching pipeline (namely Pipeline Test Set) as a second held-out test set to study the generalization ability of the marker detector.

In all cases, manual labels of marker locations were produced point-wise by a team of 5 experts, using an in-house web-based labeling tool. These locations were then transformed into pixel-wise masks by dilating them with a disc structuring element of radius r.

Results

3D Segmentation and Registration

To validate the 3D segmentation and registration, a dice coefficient was measured between the segmented 3D vessel geometry rendered as a 2D image and the 2D X-Ray roadmap of each case. The roadmap was obtained as the difference between each 2D plane image with and without injected contrast. From this difference, only the vessels are highlighted. The mean dice for both planes for all 5 cases give a value of 0.635.

Marker Detection

To evaluate the performance of the marker detection method, we measured the F1 score. Table 1 summarizes the results for marker detection in terms of F1-score (F1), precision (Pr), and recall (Re) in both of our test sets, and for each evaluated model. In all cases, a detection was considered successful if a connected component mask was located at a maximum distance of 5 pixels from the center of the ground truth marker mask.

Figure 2 depicts qualitative examples retrieved from the Pipeline test set. Notice that at least one distal marker is always found in each plane, providing enough information to approximate the current location of the device.

Distal Position Sensitivity

We conducted a sensitivity study to explore the relation between the number of detected markers and their influence on the predicted distal position along the centerline. A small sensitivity improves the stability of the pipeline result. We tested the the distal position calculation with all possible non-empty subsets of markers. The standard deviation among the subsets of markers was of 0.16 mm with a maximum difference of 0.69 mm. When measured relative to the deployed device length, the standard deviation amounted to 0.8% with a maximum difference of 1.2%. We also measured the difference between founding the 3 distal markers with founding 2 or only one. This sets were selected by moving the threshold of the marker detector

Fig. 2 Qualitative results for marker detection in the Pipeline test set
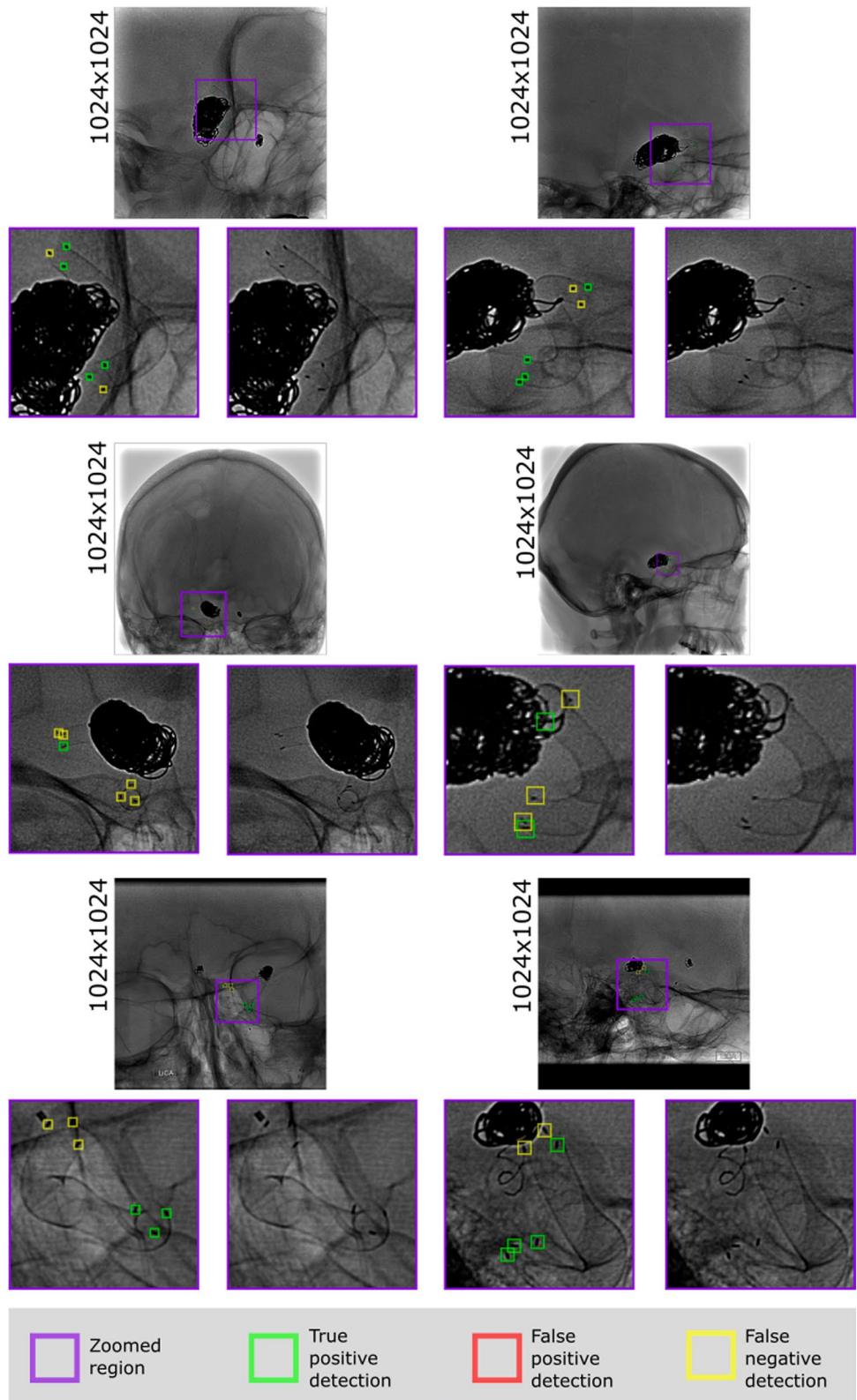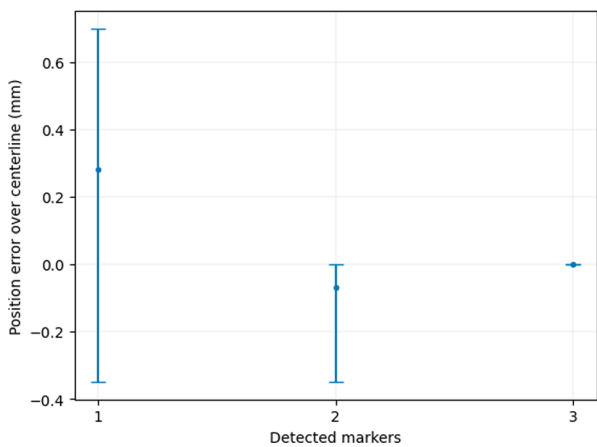
Fig. 3 Difference over the centerline abscissas (y-axis) between detecting the 3 distal markers vs 2 or 1 detected marker (x-axis)

network output until the desired number of markers are found. These results are shown in Fig. 3.

Planned vs. Intra-operative Guidance

As a use case of this method, we rendered different possible virtual FDs that are generated from the pre-operative part of the pipeline over 2D X-Ray images that are usually obtained during the treatment process. Online Resource 1 shows the 3D segmented vasculature superimposed to the 2D X-Ray images for each case of the study. By means of this strategy, we seek to enable the interventionist to assess the final position of the FD as if the device release would continue from the current state. To illustrate the convenience of this process, Fig. 4 shows three different possible
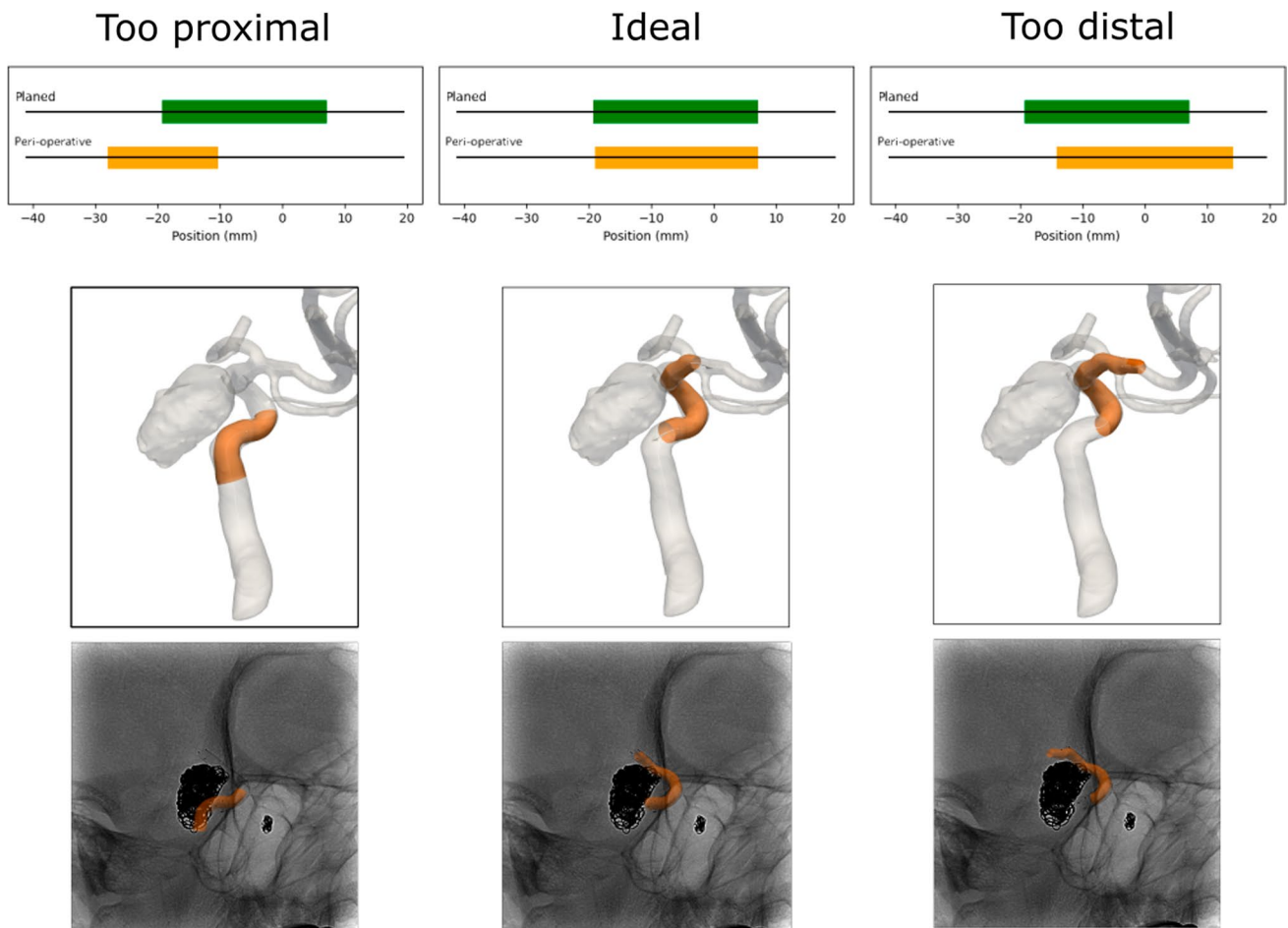
Fig. 4 Examples of online visualization of the FD location for treatment guidance. Top row: planned (green) vs peri-operative (orange) position and length of the FD. Middle row: 3D representation of the vessel and the FD. Bottom row: peri-operative 2D X-ray scan with 3D representation of the FD
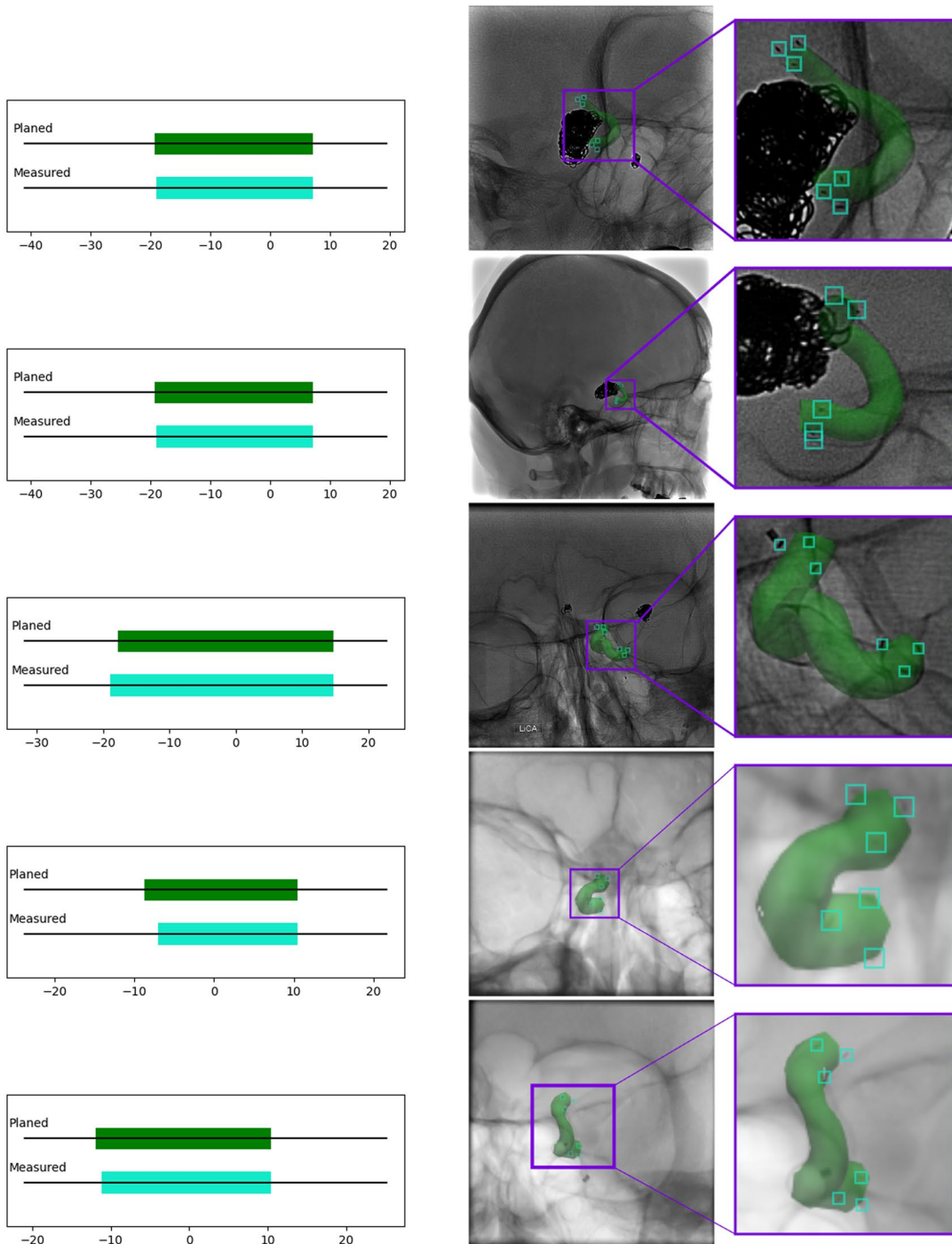
Fig. 5 Planned vs measured markers. The planned deployment is selected to match the distal markers. Distance of proximal markers are then compared to the proximal end of the FD obtained during planning

positions of deployment (i.e., on the patient) with respect to the planned one (i.e., selected by simulation), all for the same FD: one far too proximal (left), one at the ideal position chosen by the interventionist (center), and one far too distal (right). These positions would be mapped based on the locations of the distal FD markers, as detected by our CNN model. In this example, the arterial lumen becomes larger (i.e., larger vessel radius) towards the proximal end of the vessel. Therefore, positioning the FD more distally produces a longer FD than a proximal one, due to the reduced vessel radii on that region. By means of this visualization, the interventionist can adjust their decision in real-time to better accomplished the planned intervention.

Retrospective Validation

To validate the final length prediction capability of the pipeline, we gathered a retrospective collection of five datasets, each containing a 3D-DSA scan and a 2D-X-Ray biplane image displaying a deployed FD. From the post-treatment 2D images, we identified the proximal and distal markers of the implanted FD. These markers were mapped to the main vessel centerline as described in Sect. 2.4 to determine the actual 3D position of the device within the patient. We assumed the distal position markers were placed at the optimal point. Then, we simulated the final length of the FD and therefore the proximal end as explained in Sect. 2.2. The measured positions were then compared to the simulated ones which would have been obtained during treatment planning, but in this retrospective analysis were based on the distal marker positions identified in the images. Fig. 5 shows in the left column the simulated lengths vs the measured ones for each case. The right column shows the 2D X-Ray with the the markers highlighted and the simulated FD superimposed, zoomed in the region of interest. The difference along the centerline between the nearest point from the proximal FD markers and the proximal end of the FD yielded a mean difference of -0.416 mm, with a standard deviation of 0.889 mm. When considering the relative values with respect to their respective lengths, these differences correspond to a mean of $-2.3\% \pm 3.9\%$.

Frame-Rate Measurement

To be used during an intervention, this method should provide a continuous output of the current FD location as the surgery is happening. We ran the peri-operative section of the pipeline on a PC with a Intel(R) Core(TM) i7-9700 CPU, 64GB (4x16 DDR4) RAM, and a 12 GB RTX 3060 GPU. The process gave a constant throughput of 5 FPS.

Discussion

In this paper we introduced a computer-aided tool for peri-interventional guidance in intracranial aneurysm treatment, a significant stride towards enhancing procedural accuracy and interventionist decision-making.

A FD misplacement can lead to many complications[10–15]. For example, the Fig. 4 shows three different possible positions of deployment, where the final FD length changes with the vessel radii. The FD of the first column was deployed too proximal, where the final length was shorter and the aneurysm was not properly occluded. Meanwhile the third column shows a FD placed far to distal, with a larger final length, both occluding the aneurysm and a branching vessel.

The pre-operative stage of the pipeline could be done before the intervention starts, therefore it is not required to be real time efficient. While the peri-operative stage requires a low latency output from the updated input from the C-ARM device. With a throughput of 5 fps obtained by our python implementation, and a 15 fps output of a 2D X-Ray stream, the superimposed simulated FD can be updated every 3 frames. A production-ready efficient implementation of this algorithm should notably improve this performance.

Our pipeline relies on several steps, including a marker detection stage that seeks to approximate location of the FD in real-time. While our best pixel-based CNN reported poor F1 scores for detecting all possible markers, we empirically observed it was able to always identify at least one of the distal markers in images with a resolution of 1024 pixels, which is already enough to accurately approximate the distal position of the FD.

The second component of our solution is the 3D to 2D alignment of the vessel geometry, which allows to superimpose the vasculature on the 2D X-ray images for roadmapping. Prior studies have done this on other territories, such as coronaries and the aorta [27, 28, 37], providing a better understanding of where the device is been placed in the 3D space. Our alignment process was in this case purely based on the C-arm metadata. Other alternatives focused on liver vessels [38] or coronary arteries [39] involved more complex registration approaches, including deformable strategies. Adaptations of these techniques could be thoroughly applied in our context. However, the availability of C-arm information is expected considering the wide adoption of the DICOM standard.

Mapping and visualizing the FD position in real time greatly aids the interventionist during the procedure, providing augmented information about the deployment status. This has been previously reported essential to ensure more successful treatment outcomes [25]. By rendering the FD position, the interventionist can accurately assess

Fig. 6 Limitations of the marker detector algorithm in low resolution images from the Pipeline test set
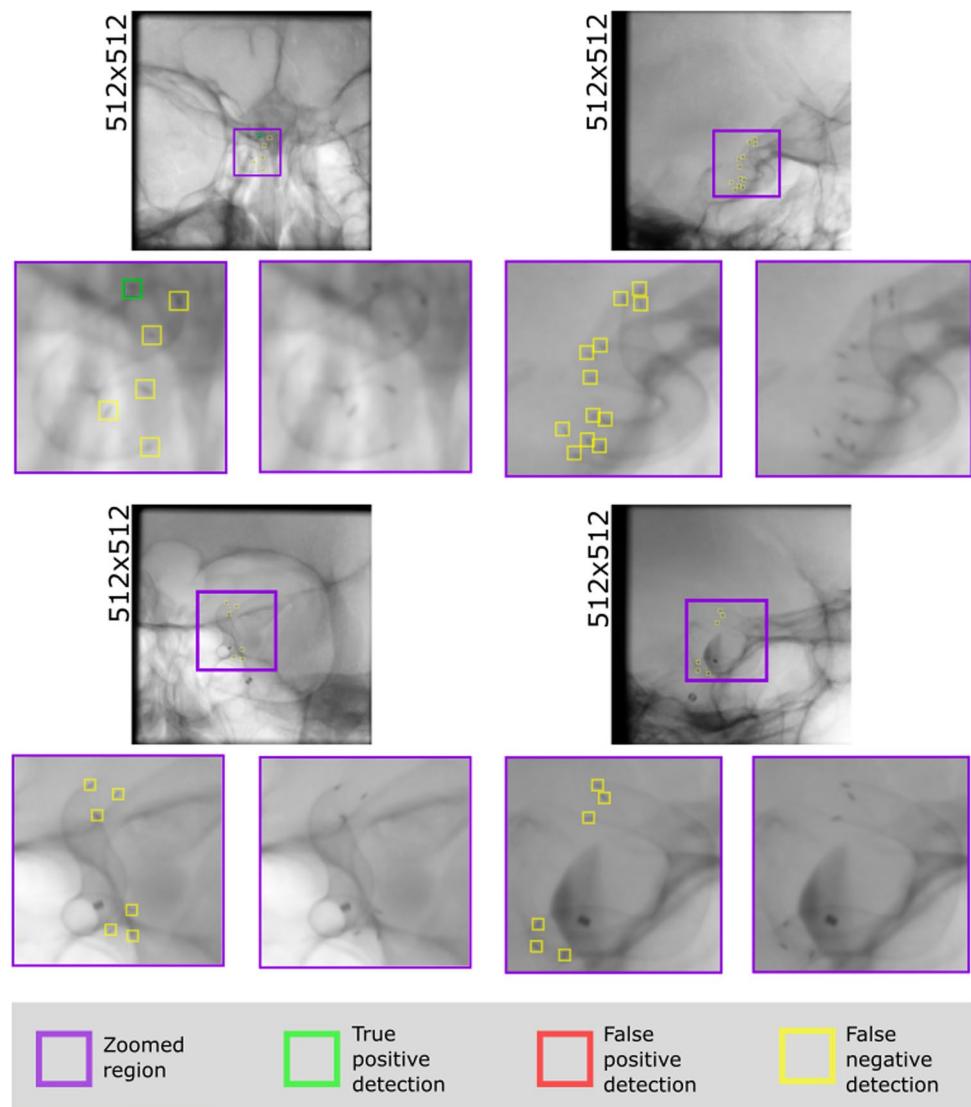
its placement, making necessary adjustments if needed. Additionally, the superimposition of the vessel geometry onto the 2D X-Ray images serves as a virtual roadmap, eliminating the need for contrast injection and offering valuable guidance throughout the procedure. This real-time augmented information enhances the interventionist's ability to make informed decisions, ultimately improving the overall safety and efficacy of the intervention.

Validating this exact approach would require to intervene patients while using this tool and quantitatively assess the final position. To simulate this scenario, we used retrospective data with already positioned FDs, and simulated an intervention in which we sought to achieve that result. In our evaluation scenario, we considered the actual FD location observed on the 2D X-Ray as the planned location. Yet, we have no indication that this was the case. Since this tool is not yet implemented in a clinical setting, it is currently not possible to to evaluate the difference between the expected position and the actual position of the device. To do this assessment, we obtained the simulated proximal marker position corresponding to the distal marker position observed on the post-treatment images. The actual proximal marker position observed on the post-treatment images was then compared to simulated proximal markers, as if the later were calculated during the planning stage. Notably, the mean difference and its standard deviation along the centerline between the nearest point from the proximal FD markers and the proximal end of the FD are close to the sensitivity of the marker detection method. This occurred even though we worked with post-treatment X-ray images, in which curved arteries looked straightened and displaced due to the placement of the FD, affecting the 3D to 2D alignment result. These

changes are not expected on real case scenarios, as the FD would not be totally expanded until the very end.

Furthermore, the observed that the spatial misfit errors of our approach are lower than the errors reported in the deployment simulation for Derivo devices ($6.83\% \pm 5.06\%$) [40]. In [40], only one projection was used to determine the position of the observed marker in 3D space. In contrast, our method takes into account two orthogonal projections, allowing for more accurate mapping of the marker position in 3D space due to its univocal solution.

Finally, the result of each step of the pipeline is crucial for the subsequent step, making no step expendable. The pre-operative steps (Vessel segmentation and virtual intervention planning), while seems unnecessary, could be done in a manual process. On the contrary, peri-operative steps need to be automated because they are time critical. This last steps are run while the patient is in surgery.

Limitations and Future Works

One of the main limitations of our work is the limited performance of our marker detector. In particular, we observed that the cases in which the model performed worse are those corresponding to low-resolution 2D X-Ray images (see Fig. 6). We believe this is likely due to the limited size and diversity of our training set, which did not include many low resolution scans. Future work should be focused on improving this specific component, either by replacing it with a more robust alternative or by increasing the quality of the training set.

Finally, another important consideration to acknowledge is that this study was conducted retrospectively using 2D X-Ray images that already contained a deployed FD. While this allowed for a comprehensive evaluation of the pipeline, it does not fully represent a real-case scenario. Ideally, future validations should involve real-time testing or utilize images specifically acquired for this purpose. By acquiring a sequence of 2D X-Ray biplane images capturing the progressive release of the distal end of the FD in different locations, a more realistic assessment of the pipeline's performance can be achieved.

Conclusion

In summary, we proposed a fully automated pipeline that combines pre- and peri-operative data to assist intracranial aneurysm treatment through the implantation of FDs. Our innovative solution aids interventionists by providing insights about the simulated treatment plan on the real-time treatment images, introducing a level of intuitive and

enhanced visualization previously unavailable. The immediate and dynamic feedback provided by our approach facilitates on-the-fly assessment of treatment progress, allowing for a direct comparison between the current procedural state and the pre-planned position. Furthermore, the inherent automation of our pipeline enhances its practicality, positioning it as a feasible and efficient tool for utilization during the intervention itself. Future work will be focused on extending the validation to new scenarios and improving the marker detection stage.

Declaration

Conflict of interest HF and LO are employees of Mentice S.L. IL is consultant for Mentice S.L. AD and RU are employees of Acandis.

Ethical Approval All procedures performed in studies involving human participants were in accordance with the ethical standards of the institutional and/or national research committee and with the 1964 Helsinki declaration and its later amendments or comparable ethical standards.

Informed Consent Informed consent was obtained from all individual participants included in the study.

References

1. Cras, T. Y., D. Bos, M. A. Ikram, M. D. Vergouwen, D. W. Dippel, T. Voortman, H. H. Adams, M. W. Vernooij, and B. Roozenbeek. Determinants of the presence and size of intracranial aneurysms in the general population: the rotterdam study. *Stroke*. 51(7):2103–2110, 2020.

2. Horikoshi, T., I. Akiyama, Z. Yamagata, and H. Nukui. Retrospective analysis of the prevalence of asymptomatic cerebral aneurysm in 4518 patients undergoing magnetic resonance angiography-when does cerebral aneurysm develop? *Neurologia Medico-Chirurgica*. 42(3):105–113, 2002.

3. Li, M.-H., S.-W. Chen, Y.-D. Li, Y.-C. Chen, Y.-S. Cheng, D.-J. Hu, H.-Q. Tan, Q. Wu, W. Wang, Z.-K. Sun, et al. Prevalence of unruptured cerebral aneurysms in Chinese adults aged 35 to 75 years: a cross-sectional study. *Annals of Internal Medicine*. 159(8):514–521, 2013.

4. Turan, N., R.A.-J. Heider, D. Zaharieva, F. U. Ahmad, D. L. Barrow, and G. Pradilla. Sex differences in the formation of intracranial aneurysms and incidence and outcome of subarachnoid hemorrhage: review of experimental and human studies. *Translational Stroke Research*. 7:12–19, 2016.

5. Frösen, J., R. Tulamo, A. Paetau, E. Laaksamo, M. Korja, A. Laakso, M. Niemelä, and J. Hernesniemi. Saccular intracranial aneurysm: pathology and mechanisms. *Acta Neuropathologica*. 123:773–786, 2012.

6. Van Gijn, J., R. S. Kerr, and G. J. Rinkel. Subarachnoid haemorrhage. *The Lancet*. 369(9558):306–318, 2007.

7. Wiebers, D. O., J. P. Whisnant, J. Huston, I. Meissner, R. D. Brown, D. G. Piepgras, G. S. Forbes, K. Thielen, D. Nichols, W. M. O'Fallon, J. Peacock, L. Jaeger, N. F. Kassell, G. L. Kongable-Beckman, and J. C. Torner. Unruptured intracranial aneurysms: natural history, clinical outcome, and risks of surgical and endovascular treatment. *Lancet*. 362(9378):103–10, 2003.

8. Lee, K. S., J. J. Zhang, V. Nguyen, J. Han, J. N. Johnson, R. Kirollos, and M. Teo. The evolution of intracranial aneurysm treatment techniques and future directions. *Neurosurgical Review*. 45(1):1–25, 2022.

9. Fiorella, D., P. Lylyk, I. Szikora, M. Kelly, F. Albuquerque, C. McDougall, and P. Nelson. Curative cerebrovascular reconstruction with the pipeline embolization device: the emergence of definitive endovascular therapy for intracranial aneurysms. *Journal of NeuroInterventional Surgery*. 1(1):56–65, 2009.

10. Tong, X., M. Han, Z. Wu, X. Feng, and A. Liu. Effects of different stent size selection on pipeline embolization device treatment of intracranial aneurysms. *Therapeutic Advances in Neurological Disorders*. 16:17562864231151476, 2023.

11. Chalouhi, N., S. Tjoumakaris, L. Gonzalez, D. Hasan, P. Pema, G. Gould, R. Rosenwasser, and P. M. Jabbour. Spontaneous delayed migration/shortening of the pipeline embolization device: report of 5 cases. *American Journal of Neuroradiology*. 34(12):2326–2330, 2013.

12. Heller, R. S., V. Dandamudi, D. Calnan, and A. M. Malek. Neuroform intracranial stenting for aneurysms using simple and multistent technique is associated with low risk of magnetic resonance diffusion-weighted imaging lesions. *Neurosurgery*. 73(4):582–591, 2013.

13. Gascou, G., K. Lobotesis, H. Brunel, P. Machi, C. Riquelme, O. Eker, A. Bonafé, and V. Costalat. Extra-aneurysmal flow modification following pipeline embolization device implantation: focus on regional branches, perforators, and the parent vessel. *American Journal of Neuroradiology*. 36(4):725–731, 2015.

14. Patankar, T., J. Madigan, J. Downer, H. Sonwalkar, P. Cowley, and F. Iori. How precise is presize neurovascular? accuracy evaluation of flow diverter deployed-length prediction. *Journal of Neurosurgery*. 137(4):1072–1080, 2022.

15. Cagnazzo, F., D. Mantilla, P.-H. Lefevre, C. Dargazanli, G. Gascou, and V. Costalat. Treatment of middle cerebral artery aneurysms with flow-diverter stents: a systematic review and meta-analysis. *American Journal of Neuroradiology*. 38(12):2289–2294, 2017.

16. Larrabide, I., M. Kim, L. Augsburger, M. C. Villa-Uriol, D. Rüfenacht, and A. F. Frangi. Fast virtual deployment of self-expandable stents: method and in vitro evaluation for intracranial aneurysmal stenting. *Medical Image Analysis*. 16(3):721–730, 2012.

17. Fernandez, H., J. M. Macho, J. Blasco, L. S. Roman, W. Mailaender, L. Serra, and I. Larrabide. Computation of the change in length of a braided device when deployed in realistic vessel models. *International Journal of Computer Assisted Radiology and Surgery*. 10(10):1659–1665, 2015.

18. Moyano, R.K., Fernandez, H., Macho, J.M., Blasco, J., San Roman, L., Narata, A.P., Larrabide, I.: A robustness test of the braided device foreshortening algorithm. In: 13th International Conference on Medical Information Processing and Analysis, vol. 10572, pp. 469–476 (2017). SPIE

19. Garcia, C., Fang, Y., Liu, J., Narata, A.P., Orlando, J.I., Larrabide, I.: A deep learning model for brain vessel segmentation in 3dra with arteriovenous malformations. In: 18th International Symposium on Medical Information Processing and Analysis, vol. 12567, pp. 61–69 (2023). SPIE

20. Zhao, J., H. Lin, R. Summers, M. Yang, B. G. Cousins, and J. Tsui. Current treatment strategies for intracranial aneurysms: an overview. *Angiology*. 69(1):17–30, 2018.

21. Paliwal, N., P. Jaiswal, V. M. Tutino, H. Shallwani, J. M. Davies, A. H. Siddiqui, R. Rai, and H. Meng. Outcome prediction of intracranial aneurysm treatment by flow diverters using machine learning. *Neurosurgical focus*. 45(5):7, 2018.

22. Dazeo, N., J. Dottori, G. Boroni, A. P. Narata, and I. Larrabide. Stenting as porous media in anatomically accurate geometries. A comparison of models and spatial heterogeneity. *Journal of Biomechanics*.110:109945, 2020.

23. Dazeo, N., R. Muñoz, A. P. Narata, H. Fernandez, and I. Larrabide. Intra-saccular device modeling for treatment planning of intracranial aneurysms: from morphology to hemodynamics. *International Journal of Computer Assisted Radiology and Surgery*. 16:1663–1673, 2021.

24. Narata, A. P., L. Obradó, R. K. Moyano, J. M. Macho, J. Blasco, A. L. Rueda, L. S. Roman, S. Remollo, C. Marinelli, R. Cepeda, et al. Cerebral aneurysm occlusion at 12-month follow-up after flow-diverter treatment: statistical modeling for v &v with real-world data. *Frontiers in Medical Technology*.3:705003, 2021.

25. Ma, D., T. M. Dumont, H. Kosukegawa, M. Ohta, X. Yang, A. H. Siddiqui, and H. Meng. High fidelity virtual stenting (hifivs) for intracranial aneurysm flow diversion: in vitro and in silico. *Annals of Biomedical Engineering*. 41:2143–2156, 2013.

26. Söderman, M., D. Babic, R. Homan, and T. Andersson. 3d roadmap in neuroangiography: technique and clinical interest. *Neuroradiology*. 47(10):735–740, 2005.

27. Goreczny, S., P. Dryzek, G. J. Morgan, M. Lukaszewski, J. A. Moll, and T. Moszura. Novel three-dimensional image fusion software to facilitate guidance of complex cardiac catheterization. *Pediatric Cardiology*. 38(6):1133–1142, 2017.

28. Bertsche, D., V. Rasche, W. Rottbauer, and I. Vernikouskaya. 3d localization from 2d x-ray projection. *International Journal of Computer Assisted Radiology and Surgery*. 17(9):1553–1558, 2022.

29. Chabi, N., Beuing, O., Preim, B., Saalfeld, S.: Automatic stent and catheter marker detection in x-ray fluoroscopy using adaptive thresholding and classification. Current Directions in Biomedical Engineering **6**(1) (2020)

30. Ramadani, A., Bui, M., Wendler, T., Schunkert, H., Ewert, P., Navab, N.: A survey of catheter tracking concepts and methodologies. Medical Image Analysis, 102584 (2022)

31. Ronneberger, O., Fischer, P., Brox, T.: U-net: Convolutional networks for biomedical image segmentation. In: Medical Image Computing and Computer-Assisted Intervention–MICCAI 2015: 18th International Conference, Munich, Germany, October 5-9, 2015, Proceedings, Part III 18, pp. 234–241 (2015). Springer

32. Vernikouskaya, I., D. Bertsche, T. Dahme, and V. Rasche. Cryoballoon catheter localization in x-ray fluoroscopy using u-net. *International Journal of Computer Assisted Radiology and Surgery*. 16:1255–1262, 2021.

33. Huang, L., Liu, Y., Chen, L., Chen, E.Z., Chen, X., Sun, S.: Robust landmark-based stent tracking in x-ray fluoroscopy. In: Computer Vision–ECCV 2022: 17th European Conference, Tel Aviv, Israel, October 23–27, 2022, Proceedings, Part XXII, pp. 201–216 (2022). Springer

34. Isensee, F., P. F. Jaeger, S. A. Kohl, J. Petersen, and K. H. Maier-Hein. nnu-net: a self-configuring method for deep learning-based biomedical image segmentation. *Nature Methods*. 18(2):203–211, 2021.

35. Antiga, L., M. Piccinelli, L. Botti, B. Ene-Iordache, A. Remuzzi, and D. A. Steinman. An image-based modeling framework for patient-specific computational hemodynamics. *Medical & Biological Engineering & Computing*. 46(11):1097–1112, 2008.

36. Hervella, Á. S., J. Rouco, J. Novo, M. G. Penedo, and M. Ortega. Deep multi-instance heatmap regression for the detection of retinal vessel crossings and bifurcations in eye fundus images. *Computer Methods and Programs in Biomedicine*.186:105201, 2020.

37. Ambrosini, P., I. Smal, D. Ruijters, W. J. Niessen, A. Moelker, and T. Van Walsum. A hidden markov model for 3d catheter tip tracking with 2d x-ray catheterization sequence and 3d rotational angiography. *IEEE Transactions on Medical Imaging*. 36(3):757–768, 2016.

38. Ambrosini, P., D. Ruijters, W. J. Niessen, A. Moelker, and T. van Walsum. Continuous roadmapping in liver tace procedures using 2d–3d catheter-based registration. *International Journal of Computer Assisted Radiology and Surgery*. 10(9):1357–1370, 2015.

39. Wu, W., Zhang, J., Peng, W., Xie, H., Zhang, S., Gu, L.: Car-net: A deep learning-based deformation model for 3d/2d coronary artery registration. IEEE Transactions on Medical Imaging (2022)

40. Narata, A. P., J. Blasco, L. S. Roman, J. M. Macho, H. Fernandez, R. K. Moyano, R. Winzenrieth, and I. Larrabide. Early results in flow diverter sizing by computational simulation: quantification of size change and simulation error assessment. *Operative Neurosurgery*. 15(5):557–566, 2018.